PILATUS: A 2-Dimensional Detector for Protein Crystallography

E.F. Eikenberry[a], *Ch. Broennimann*[a], *G. Huelsen*[a], *H. Toyokawa*[b], *R. Horisberger*[c], *B. Schmitt*[a], *C. Schulze-Briese*[a], *and T. Tomizaki*[a]

[a]*Swiss Light Source (SLS), WSLA/218, Paul Scherrer Institute (PSI), CH-5232 Villigen-PSI, Switzerland.*
[b]*Japan Synchrotron Research Institute, 1-1-1 Kouto, Mikazuki-cho, Sayo-gun, Hyogo 679-5198, Japan.*
[c]*Paul Scherrer Institute, CH-5232 Villigen-PSI, Switzerland.*

Keywords: X-ray crystallography; Pixel detector; Single photon counting; Fine slicing

1 Abstract

A large area all-silicon counting pixel detector for protein crystallography is being developed at the SLS. The detector is of modular design, with the final detector envisaged to have at least 2k x 2k pixels covering an area of *ca.* 40 x 40 cm^2. To date, eight modules have been constructed, each consisting of an 80 x 34 mm^2 monolithic silicon sensor with a 2 x 8 array of custom CMOS readout chips bump-bonded to it. The readout chips have a 44 x 78 array of 217 x 217 μm^2 pixels, each with a 15-bit counter. Experiments with crystals of the protein lysozyme carried out at beamline 6S of the SLS demonstrated the suitability of a prototype of this detector for demanding experiments in which the fine ϕ-sliced mode of data collection is utilized. To improve yield, speed and dynamic range, the readout chip has been redesigned in a 0.25 μm CMOS process. Preliminary tests show that this chip works well, and should be able to count up to 10^6 x-rays/s/pixel.

2 Introduction

X-ray crystallography is today the most popular method for the determination of molecular structure at atomic resolution. Such structures are widely sought for drug design, research on basic cellular mechanisms, and in the burgeoning field of structural genomics.

In this method, a small crystal comprised of the molecules under study is rotated in a beam of, typically, 12 keV x-rays, and the resulting diffraction patterns are recorded by a detector placed behind the specimen. A beamstop shields the detector

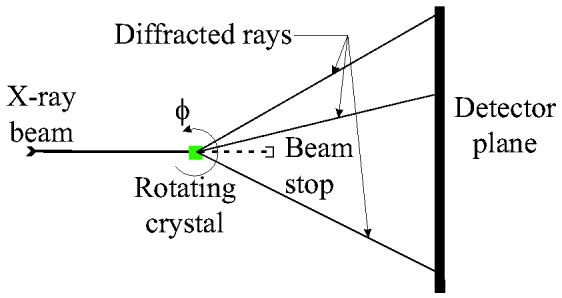

Figure 1: Experimental setup for macromolecular crystallography. A nearly parallel beam of X-rays from the synchrotron is diffracted by the specimen to form a diffraction pattern which is recorded by the detector. The specimen, typically cryogenically cooled to mitigate x-ray irradiation damage, is rotated in the beam about the so-called ϕ-axis (perpendicular to the page) to permit sampling of the full volume of the reciprocal space defined by the crystal.

from the undiffracted direct beam [Figure 1]. The crystal is rotated by *ca.* 1° about its ϕ-axis while the detector records the diffraction pattern as an image frame. Software packages are available to analyze the positions and intensities of the recorded patterns of Bragg maxima (reflections) to give the desired structure. A full data set for an average protein contains hundreds or even thousands of images with a total of 10^5 to 10^6 or more reflections. The protein data bank now contains more than 19,000 structures solved in this way [1].

Third-generation synchrotron x-ray sources, such as the Swiss Light Source, offer users small diameter, high intensity and low emittance x-ray beams that are ideally suited for determining the structures of large molecules by crystallography. Because of these optical properties, most users find that data collected at the synchrotron are of higher quality, and extend to higher resolution, than data collected from comparable crystals on a laboratory x-ray source.

Charge-coupled device (CCD) based detectors are currently the preferred devices for data collection on macromolecular crystallography beamlines at synchrotron sources. These detectors consist of an energy-converting phosphor screen optically coupled to a large area CCD by means of a fiber optic taper [2]. Mosaic arrays of 9 or 16 CCDs covering areas as large as 315 x 315 mm^2 are available. These detectors are excellent in most respects, but have a few drawbacks: *viz.*, a large point-spread function (PSF) which smears out the data, a relatively long readout time (1-3 s), significant read-out noise (*ca.* two 12 keV x-rays), and a limited dynamic range (typically $< 10^4$).

The readout time limitation, in particular, makes it impractical to do fine ϕ-sliced data acquisition. In this mode of operation, the crystal is rotated in very fine

steps (*e.g.*, 0.02°) about its spindle axis, and a diffraction image is collected in the small angular range at each position. Several theoretical studies, backed by limited experimental evidence, suggest that this mode should give improved signal-to-noise ratios in the integrated intensities of Bragg reflections, thereby leading to improved structures [3] [4]. However, collecting a full 180° fine ϕ-sliced data set, required for low-symmetry crystals, is not feasible with present detectors because of the time required, and because the read noise compromises the potential improvement.

To address the limitations of current devices for macromolecular crystallography and medical imaging applications, we and several other groups are developing all-silicon hybrid pixel detectors that operate in single photon counting mode [5] [6] [7] [8] [9] [10]. By comparison to CCD detectors, pixel detectors have negligible PSF and readout noise, fast readout, and improved dynamic range.

3 Design and Fabrication

The design of the SLS detector has been described previously [5] [11]. Briefly, the final detector is to be an assembly of 60 modules covering an area of *ca.* 40 x 40 cm^2 and representing at least 2k x 2k pixels. Each module is comprised of a single monolithic silicon sensor bump-bonded to an 8 x 2 array of custom CMOS readout chips. The sensor is 300 μm thick and is patterned into an array of 366 x 157 pixels, each 217 x 217 μm^2, giving a sensitive area of 79.4 x 34.1 mm^2 [Colibrys, Neuchâtel, Switzerland]. Through the use of double-sized and quad-sized pixels at the chip boundaries, there is no dead area in the module. The readout chips, designed at SLS, are fabricated in the radiation tolerant 0.8 μm DMILL process and have a format of 44 x 78 pixels [Atmel-Temic, Nantes, France]. Each pixel contains a preamplifier, a shaper, a threshold comparator and a 15-bit pseudo-random shift-register counter. A 4-bit DAC is provided in each pixel to adjust the comaprator threshold together with a circuit to inject a calibration pulse at the amplifier input. The pixels are individually addressable, which has been of great value for testing, calibration and overcoming the high pixel defect rate (see below). The bump-bonding is done with Indium balls 17-20 μm diameter and is done at SLS. At room temperature, the preamplifier has ENC of *ca.* 75 e^-, which permits x-rays of energy from *ca.* 5 to > 20 keV to be recorded in single-photon counting mode, the upper limit being set by the stopping power of the sensor.

Each module has a module control board (MCB) to carry the associated electronics. Two types of modules have been fabricated: angle-bracket modules (with electronics perpendicular to the sensor) which will be tiled to constitute the final detector; and flat modules for testing, which can be butted only laterally. To date, eight modules have been fabricated and tested. The first angle-bracket modules utilized a kapton high-density interconnect (Hightec MC, Lenzburg, Switzerland) onto which

the bump-bonded module was adhered, and which was bent at right-angles to mate to the MCB. Connections between the CMOS chips, the kapton interconnect, and the MCB were made by wire-bonding. This difficult assembly will shortly be replaced with a monolithic flexible hybrid circuit (Dyconex, Zurich, Switzerland) which will considerably reduce the required number of wire bonds. Three flat modules butted laterally were used to build a single bank detector with a format of 1120 x 157 pixels, covering an area of 24.3 x 3.4 cm^2 [Figure 2]. Two spaces between the modules, each 11 pixel columns wide, is included in these figures, so the active pixel count in the horizontal direction is 1098. The modules are connected to a bank control board (BCB) via short adapter cards that in the final detector will pass through slots in the water-cooled carrier plate for the banks.

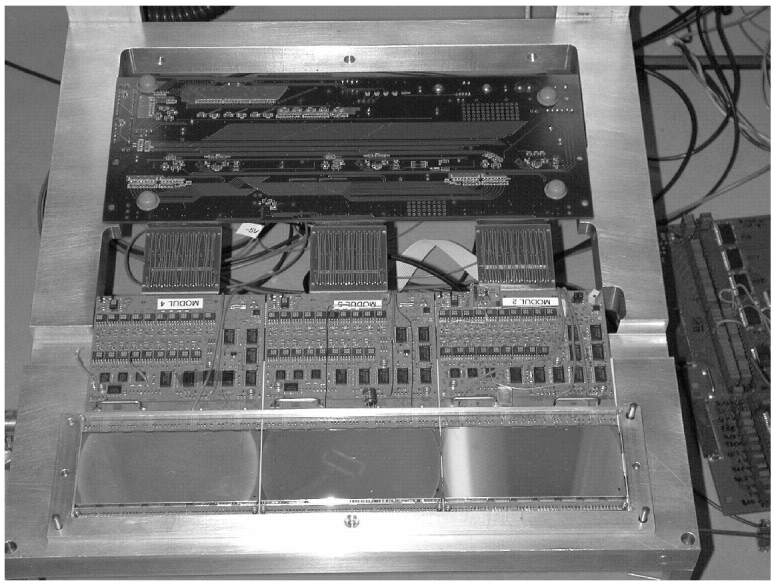

Figure 2: The single-bank detector consisting of 3 flat modules. The sensors are seen in the foreground. The BCB is seen at the rear connected to the modules by 3 adapter cards.

Signals to operate the detector are generated by two 16-bit VME pattern generators (Dipl.-Ing. Kramert, Remigen, Switzerland). All chips are read out in parallel, thus the readout time does not scale with the detector size. At 10 MHz the readout time is 6.7 ms, during which data are moved to FIFO (first-in first-out) memories on the BCB. The pixel counters are then re-enabled while data are moved from the BCB through a VME FIFO to the host computer, a commodity PC with GNU/Linux. The latter transfer will become rate-limiting for a larger detector, and the VME FIFO will shortly be replaced by a PCI card in the computer, which will take data directly from the detector to computer memory space. The two halves of the detector will be

serviced by independent computers, so that at the maximum planned framing rate of 10 images/s (giving a minimum exposure time of 100 ms, in agreement with the expected exposure time for many crystals in the fine ϕ-sliced mode), the data rate will be *ca.* 40 Mbyte/s for each computer. The software to operate the detector is custom-designed and splits control into two components: a relatively simple image server which is attached to the hardware, and a complex control program that provides arbitrary sequences of commands for data acquisition, analysis or testing. With this arrangement, control of the image server, after setting up, can be easily given over to the beamline software for data taking.

Figure 3: Flat-field corrected image of Br fluorescence x-rays (11.9 keV) recorded with the single bank detector. The 11 pixel gaps between the modules are seen as black columns. Black pixels are defective. Three chips have partial or total electrical or bump-bonding failure. The flat field correction takes into account air absorption, angle-of-incidence correction, and silicon absorption. Each pixel received 1.2 x 10^4 x-rays in this 40 s exposure. The left and right edges of the image are slightly darkened because of the $1/r^2$ falloff of the illuminating field.

4 Testing

The single bank detector [Figure 2] has been extensively tested in the laboratory and at beamline 6S of the SLS, the protein crystallography beamline [14]. Figure 3 shows a flat-field corrected image of Br fluorescence radiation emitted from a solution of KBr illuminated with 13.5 keV x-rays. The 11.9 keV fluroescence is near the energies most used by experimenters at the synchrotron and is thus ideal for calibration. Most of the pixels respond perfectly, but defects of three kinds are seen. Individual defective pixels (black) are caused by yield problems in the CMOS chips and by defective bump bonds. Currently we find 3.5% of pixels in selected good chips to be defective (2.9% digital defects, 0.6% analog defects). About 0.4% of individual defects are in the bump bonds. Pixels surrounding defective bumps frequently have elevated signal levels because of charge-sharing. A second class is area defects, which are bump-bonding errors caused either by alignment problems or particulate contaminants, which prevent proper apposition of the surfaces. These problems are being reduced through experience; indeed, the central module in Figure 3 is one of the more recent.

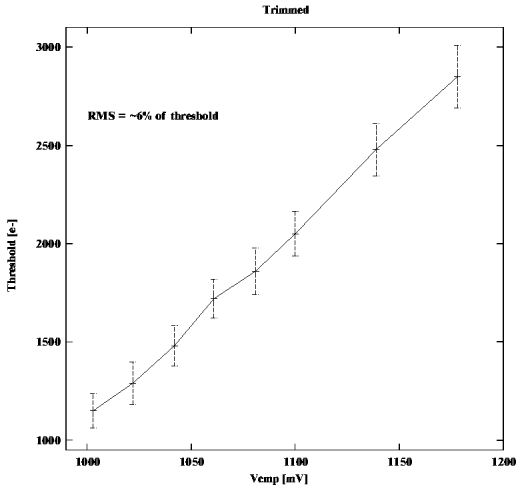

Figure 4: Average trimmed threshold levels and dispersion as a function of comparator setting for a module after the threshold adjustment procedure. To adjust the pixels, the calibration pulse amplitude is fixed at the desired value (ideally corresponding to half of the x-ray energy), and, with DAC settings all 0, the global comparator voltage, V_{cmp}, is adjusted until essentially all good pixels are counting. This sets the floor of the trim range. The range is set by setting all DACs to 15 and increasing the trim strength (called V_{trim}) until most pixels are no longer responding. Images of calibration pulses are made at each of the 16 possible DAC settings, and the optimum setting is selected by exhaustive search of the images for the setting at which each pixel records half of the calibration pulses. After setting the DACs, the dispersion is calculated from a threshold scan of each pixel. The procedure takes only a few minutes. The values are saved for loading as needed for different energies used during an experiment.

A third class is random "hot" pixels (bright pixels, which are not possible to see in the illustration) which are counting errors that arise when two x-rays, by chance, are spaced 300-400 ns apart in time. Such a situation is guaranteed by the interval (Poisson) distribution of the arrival times of x-rays, but was not seen in laboratory testing until we used random noise as input instead of regular pulses. Though rare, the frequency of occurrence of this problem increases linearly with the average counting rate; with 172,386 pixels, a few pixels display false values already at an average of a few hundred x-rays/s/pixel. But because the occurrence is random, it is possible to correct the errant pixel values using replicated images with the techniques for "dezingering" CCD images [12].

Procedures were developed to trim the thresholds of the pixels using calibration pulses. Before trimming, the average threshold dispersion of the chips was 15%. Trim-

ming inevitably increased the threshold, but reduced the dispersion to 6%. A feature of the comparator design is that the dispersion scales linearly with the threshold, thus allowing levels as low as 5 keV, or lower, to be set [Figure 4]. It is planned to test the validity, uniformity and stability of the settings with x-rays.

5 Crystallography Tests

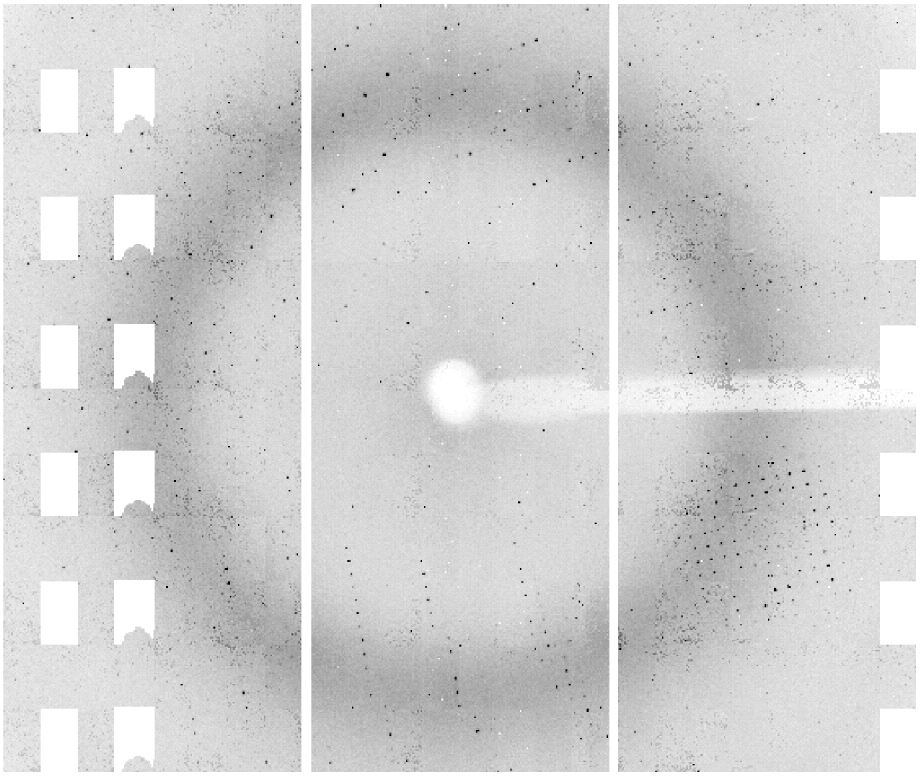

Figure 5: Diffraction from a cryogenically cooled crystal of hen egg white lysozyme during a 1° rotation. The x-ray energy was 11.9 keV, corresponding to a wavelength of 0.104 nm, and the exposure time was 2 s. X-rays are dark. The prominent ring derives from the water in the specimen. The high mosaicity of the crystal, *ca.* 0.36°, leads to the rather large Bragg spots seen here. A better crystal would have many spots confined essentially to single pixels, and consequently nearly invisible in illustrations. (Please magnify or print the image to see the Bragg spots.)

Crystallography experiments with the single bank detector were also made at beamline 6S of the SLS with frozen crystals of the enzyme lysozyme. Figure 5 shows a 1° rotation pattern from a set of 90 images covering 90° rotation. For a crystal of

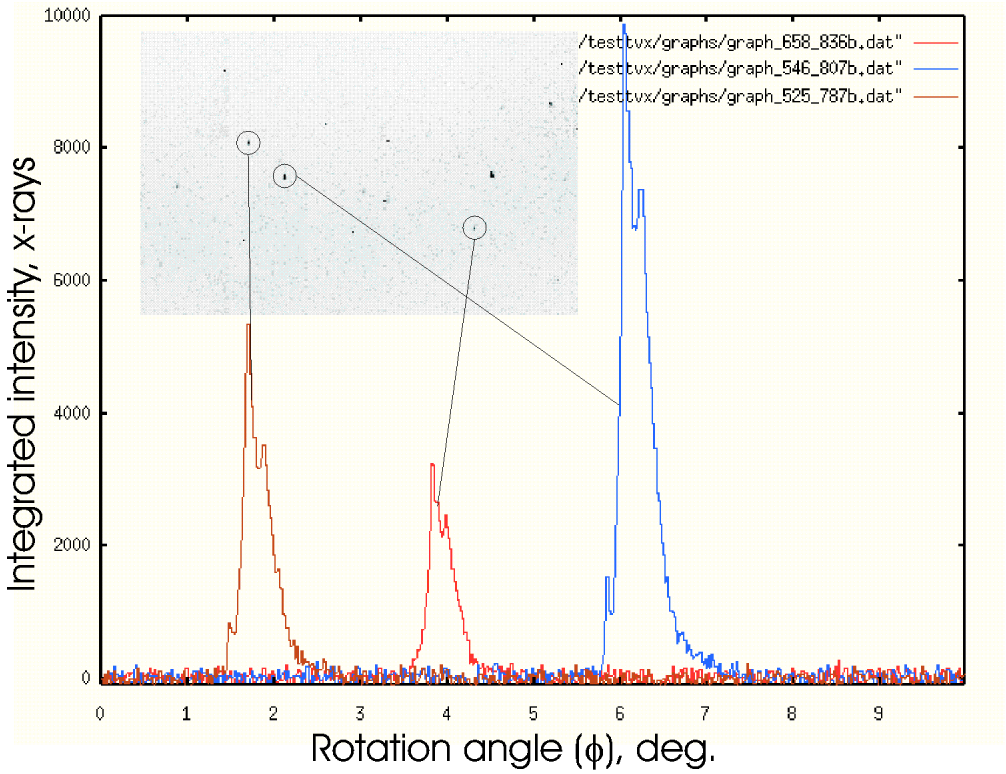

Figure 6: Fine ϕ-sliced data collection with continuous sample rotation. The experimental setup is the same as Figure 5. During the 10° rotation the x-ray shutter was open continuously and 500 images, each of 0.5 s duration, were recorded. The image (inset) corresponds to the lower central part of Figure 5. The graphs show the integrated intensity of the 3 indicated spots over the 10° rotation. The detailed similarity of the 3 profiles shows that these complex profiles result from the mosaic structure of the crystal.

this symmetry (orthorhombic space group $P2_12_12$), 90° constitutes a complete data set (*i.e.*, all possible reflections are recorded at least once). To record these images, the detector was translated vertically through each of 6 positions using the high precision stage at the beamline. At each position the sample was reset to the starting orientation, and the rotation set was repeated. The resulting images have a format of 1120 x 942 pixels covering an area of 24.3 x 20.4 cm^2. These data were recorded in the traditional start/stop mode in which the crystal is positioned slightly behind the desired angular starting point, then accelerated to the correct angular speed. When the crystal reaches the correct starting point, the shutter is opened for the required time, then the crystal is decelerated and rewound to the starting point for the next exposure.

Data were also recorded in the fine ϕ-slicing mode with the shutter continuously open, using the detector to define the exposure time. This is a much more efficient use of the x-ray beam, and of the limited crystal lifetime, than the start/stop mode of operation. The crystal was rotated 10°, during which 500 exposures were recorded, each with an exposure time of 0.5 s. Thus, each image comprised a rotation of 0.02°. The total time lapse at each position was 262 s, giving a duty cycle of >95%. As before, the detector was translated vertically through 6 positions to record the full images. Figure 6 shows a 300 x 300 pixel section from the lower central part of the images, together with an integrated intensity profile of 3 selected Bragg spots. The readout time of the detector has subsequently been optimized to 6.7 ms, which gives a duty cycle >98.5% in 0.5 s exposures.

6 Data Processing

The initial steps in solving a crystal structure from crystallographic data include finding the center of each Bragg reflection, determining the orientation of the crystal in the x-ray beam, indexing the reflections (assigning unique reciprocal space indices to each Bragg maximum in each image), determining the space group, determining the unit cell parameters of the space group, and calculating the integrated intensity of each reflection together with certain statistics. A number of program packages are available to carry out these complex calculations as well as the subsequent steps that lead to a structure. We are working with a popular open-source package, MOSFLM, which permits us to adjust certain routines to work better with pixel detector data [13].

The pixel detector data have several properties that cause such packages considerable problems. First is the defective pixels, which badly mislead the Bragg spot-finding algorithm. This has been circumvented by filling in the known bad pixels with average values for the respective parts of the pattern, as has been done in Figure 5. The unexpected geometry of the detector together with the very sharp point spread function also causes problems. The algorithms expect the spot positions to have been corrected to geometrically exact positions, as is done with CCD detectors. In the case of the pixel detector, the spots are in geometrically perfect positions, limited only by the precision of photolithography, within one module, but between modules there is a significant alignment error, which can be corrected to less than 1 pixel. In CCD images, where the spots are smeared by a significant point spread function (PSF), the center of gravity of a spot can be adjusted by a fraction of a pixel [12]. But, with the pixel detector, which has essentially zero PSF, this doesn't work well. We are modifying the geometry algorithm in the program suite to take into account the measured relative positions of the modules. The problem of the "hot" pixels in fine ϕ-sliced data can be dealt with by standard curve-fitting procedures because they stand our sharply in the angle scans. MOSFLM was successful at processing the data

set of Figure 5 though more optimization remains to be done.

7 Deep Sub-micron Design

To increase the speed and dynamic range of the readout chip, and to reduce or eliminate the problem of defective pixels, we have ported the chip design to the 0.25 μm CMOS process available through EuropracticeIC (Imec, Leuven, Belgium). The major concepts of the pixel described above are retained. A custom design library based on enclosed-gate transistors (developed at PSI), in combination with the inherent properties of the thin oxide used in this process, ensures a radiation tolerant design [15]. The new pixel is 172 x 172 μm^2, has a 20-bit counter, a 6-bit DAC for threshold adjustment and is designed for a 100 MHz readout clock. The chip will have a 56 x 99 pixel format which gives a readout time of *ca.* 1.1 ms. The 20-bit pseudo-random shift register counter is a fully static design, rather than half-dynamic (which accounted for some of the digital failures in the present chip). A pulse generator acts on the output of the comparator to provide uniform pulses to the counter.

The first prototype chips, without trim DACs, have been received and tested. With calibration pulses and mid-range settings of the preamplifier and shaper time constants, the chip counts well at 2 MHz, suggesting that with optimized settings x-ray rates approaching 1 MHz could be accepted with some dead-time correction. The prototypes of the full pixel, with trim bits and redesigned pulse generator are expected in Februrary, 2003.

8 Acknowledgements

The authors gratefully acknowledge the assistance of F. Glaus, J. Rothe, and S. Streuli in fabricating modules, C. Buehler for developing the BCB and C. Pradervand for helping to set up beamline 6S of the SLS. G.H. acknowledges support from the Swiss National Science Foundation.

References

[1] *see* http://www.rcsb.org/pdb/.

[2] S.M. Gruner, E.F. Eikenberry, and M.W. Tate. Rev. Sci. Instrum. 73, 2815-2842 (2002).

[3] J.W. Pflugrath. Acta Cryst., D55, 1718-1725 (1999).

[4] W. Kabsch. International Tables for X-ray Crystallography, vol. F. M.G. Rossmann and E. Arnold, eds. Kluwer Academic Publishers, Dordrecht, 2001, pp. 218-225.

[5] Ch. Broennimann, R. Baur, E.F. Eikenberry, S. Kohout, M. Lindner, B. Schmitt, and R. Horisberger. Nucl. Instrum. Meth. Phys. Res. A 465, 235-239 (2001).

[6] J.-F. Berar, L. Blanquart, N. Boudet, P. Breugnon, B. Cailot, J.-C. Clemens, P. Delpierre, I. Koudobine, C. Mouget, R. Potheau, and I. Valin. J. Appl. Cryst. 35, 471-476 (2002).

[7] B. Mikulec, M. Campbell, G. Dipasquale, C. Schwarz, and J. Watt. Nucl. Instrum. Meth. Phys. Res. A, 458, 352-359 (2001).

[8] P. Datte, A. Birkbeck, E. Beauville, N. Endres, F. Druillole, L. Luo, J. Millaud, and N.-H. Xuong. Nucl. Instrum. Meth. Phys. Res. A, 421, 576-590 (1999).

[9] M.S. Passmore, R. Bates, K. Mathieson, V. O'Shea, M. Rahman, P. Seller, and K.M. Smith. Nucl. Instrum. Meth. Phys. Res. A, 466, 202-208 (2001).

[10] C. Ponchut, J.L. Visschers, A. Fornani, H. Graafsma, M. Maiorino, G. Mettivier and D. Calvet. Nucl. Instrum. Meth. Phys. Res. A, 484, 396-406 (2002).

[11] Ch. Broennimann, R. Baur, E.F. Eikenberry, P. Fischer, S. Florin, R. Horisberger, M. Lindner, B. Schmitt, and C. Schulze. Nucl. Instrum. Meth. Phys. Res. A 477, 531-535 (2002).

[12] S.L. Barna, M.W. Tate, S.M. Gruner and E.F. Eikenberry. Rev. Sci. Instrum., 70, 2927-2934 (1999).

[13] *see* http://www.ccp4.ac.uk/.

[14] *see* http://x06sa.web.psi.ch/.

[15] W. Snoeys, F. Faccio, M. Burns, M. Campbell, E. Cantatore, N. Carrer, L. Casagrande, A. Cavagnoli, C. Dachs, S. Di Liberto, F. Formenti, A. Giraldo, E.H.M Heijne, P. Jarron, M. Letheren, A. Marchioro, P. Martinengo, F. Meddi, B. Mikulec, M. Morando, M. Morel, E. Noah, A. Paccagnella, I. Ropotar, S. saladino, W. Sansen, F. Santopietro, F. Scarlassara, G.F. Segato, P.M. Signe, F. Soramel, L. Vannucci, and K. Vleugels. Nucl. Instrum. Meth. Phys. Res. A, 439, 349-360 (2000).